PAPER

Check for updates

One-pot fabrication of ferric ferrocyanide functionalized graphene hydrogel for cesium removal in aqueous solution

Yan-Rong He, Yang Yang, Zhao-Ya Huang, Wei-Juan Wang, Xiao-Long Li, Peng-Hao Zhang, Zhao-Yi Tan* and Dong Zhang (ID) *

The rapid development of the nuclear industry brings benefits for global economic development and solves the energy crisis. However, nuclear industrial activities produce a large amount of radioactive wastewater, which poses serious threats to environmental safety and human health, and ^{137}Cs is considered one of the most abundant radionuclides in radioactive wastewater. In this study, we fabricated a new type of ferric ferrocyanide (Prussian blue, PB) functionalized graphene hydrogel (PB/rGOH) for Cs(I) removal. The as-prepared PB/rGOH shows a three dimensional network with PB nanoparticles uniformly distributed on the surface of the rGO sheets. The PB/rGOH could be readily separated from aqueous solution. Moreover, the volume of the composite could shrink to a small stiff bulk material, further reducing the volume of the waste. Kinetics experiments showed that Cs(I) adsorption on PB/rGOH fitted well with pseudo-second-order kinetic model, and the equilibrium data agreed well with the Langmuir model. As calculated from the Langmuir model, the maximum adsorption capacity at pH 5.0 is 58.82 mg g^{-1}. The increase of pH from 3 to 7 could enhance the adsorption capacity, however, further increasing the pH value resulted in serious decomposition of PB nanoparticles. In conclusion, the PB/rGOH prepared in our work showed good performance on removal of Cs(I) in aqueous solution, and has a good application prospect in radioactive waste water treatment.

Introduction

Currently, global climate change and fossil fuel depletion have impelled more and more countries to develop alternative clean energy. Nuclear power, which supplied about 4.8% of the world's energy in 2014, is widely considered as a sustainable solution to the global energy crisis.[1,2] However, nuclear industrial activities pose many threats to the environment and human health due to the release of large amounts of radioactive wastewater, including radioactive waste leaking from tanks and released during nuclear power plant accidents.[3,4] For example, in the Fukushima accident on March 11, 2011, huge amounts of radionuclides such as ^{134}Cs, ^{137}Cs, ^{131}I, and ^{90}Sr were released into the water, air, and land, and the control and removal of radioactive wastes from polluted water and soil have been gaining interest world wide.

According to previous researches, the direct release of ^{137}Cs into the environment is considered as one the most abundant radionuclide.[5] Being one of the most hazardous contaminants, ^{137}Cs has a long half-life of 30.1 years and emits beta-particles and strong gamma rays.[6] In addition, based on its chemical similarity to potassium, Cs(I) has high solubility and could

Institute of Nuclear Physics and Chemistry, China Academy of Engineering Physics, Mianyang, 621000, China. E-mail: tanzhaoyi@caep.cn; zd0823@caep.cn
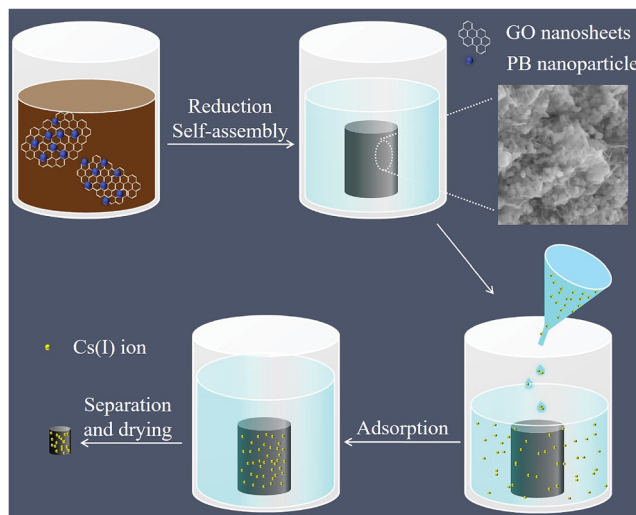
favorably migrate through groundwater to the food chain.[7] Thus, it is necessary to develop an effective extraction process to remove the radioactive Cs(I) from wastewater. Ferric ferrocyanide (Prussian blue, PB) and its analogous hexacyanoferrate compounds are well-known adsorbents for the selective removal of cesium ions owing to its radiation stability, high adsorption capacity, low-cost and biocompatibility. PB has been effectively used to treat Cs(I) exposure after the Chernobyl nuclear reactor disaster and the Goiania accident.[8,9] However, to maintain a high adsorption capacity, PB is usually in the form of a very fine powder, which makes it difficult to be separated from aqueous solutions by filtration or centrifugation after Cs(I) sorption. In addition, these small particles cannot be directly used in fixed-bed columns due to the pressure and clogging. To address these problems, numerous studies have been dedicated to the immobilization of PB nanoparticles in porous materials or at the surface of structural materials.[7,8,10–15] Fox example, Jang *et al.* bound PB nanoparticles to the core of magnetite (Fe$_3$O$_4$) nanoparticles, achieving highly efficient and rapid separation of Cs(I) from aqueous solution.[13]

In recent years, graphene hydrogels and aerogels have received more and more attentions because of their large surface area, high conductivity, excellent mechanical flexibility and chemical stability.[16,17] The porous network and large surface area make graphene hydrogels/aerogels effective

Fig. 1 Schematic of approach for PB/rGOH and Cs(I) removal.

support materials for nanoparticle dispersion.[18–21] Adhikari *et al.* prepared metal nanoparticles containing graphene hybrid hydrogel as a potential catalyst for the reduction of aromatic nitro to amino group.[22] Zhang *et al.* fabricated graphene-based nanohybrid material to support Pd nanoparticles and obtained uniformly distributed Pd nanoparticles on the surface of graphene sheets.[23] In our previous work, we found that after air dried, graphene hydrogel could shrink to form graphite-like bulk materials, accompanying with a significant volume reduction. Such a volume reduction is beneficial to waste minimization. Therefore, graphene hydrogel could be a promising support material for utilizing PB nanoparticles for Cs(I) removal in radioactive wastewater.

Based on the above, in this study, we fabricated PB nanoparticles functionalized graphene hydrogel (PB/rGOH) and developed a new approach to remove Cs(I) from aqueous solution as shown in Fig. 1. The PB/rGOH was fabricated by reducing graphene oxide (GO) using ascorbic acid in the presence of PB nanoparticles. The physical and chemical properties of the prepared materials were characterized, Cs(I) adsorption performance of PB/rGOH were determined, and the application prospect of the material in radioactive wastewater treatment was estimated.

Experimental

Fabrication of PB/rGOH

GO was prepared by oxidizing nature graphite powder (325 mesh) using a modified method as described previously.[24] In our work, aqueous suspensions of GO with a concentrations of 1.5 mg mL^{-1} was used. PB nanoparticles, purchased from Aladdin Industrial Co., China, were ultrasonically dispersed in deionized water for about 24 hours prior to use, with a concentration of 15 mg mL^{-1}. To prepare PB/rGOH: 4 mL of GO suspensions, 0.4 mL of PB suspension, 1 mL of ascorbic acid (42 g L^{-1}), and 1.6 mL of distilled water were mixed into a glass bottle with a volume of 10 mL, then the mixed suspension was heated at 60 °C for 5 h. To obtain PB/rGOH with different PB/GO (w/w) ratios, the conditions was maintained as the above, except

that the volumes of PB suspension was 0, 0.2, 0.4, 0.8, 1.2, 2.0 mL, respectively. Afterwards, the total volume of the mixture were supplemented to 7 mL with deionized water. The as-prepared materials were dialyzed against deionized water for 2 days to remove residual micromolecules prior to use. As control subject, rGOH was fabricated by the same step except that deionized water was used to replace the PB suspension.

Characterization of PB/rGOH

Scanning electron microscope (SEM, Ultra 55, Carl Zeiss Ltd., Germany) was used to characterize the morphology of the PB/rGOH. Transmission electron microscopy (TEM) images of the PB/rGOH were obtained on a Libra 200FE instrument (Carl Zeiss Ltd., Germany). X-ray photoelectron spectroscopy (XPS) tests were conducted using an ESCALAB 250 instrument (Thermo-VG Scientific Inc., USA). The XPS data were analyzed with curve-fitting software (XPSPEAK v4.1). X-ray diffraction (XRD) tests were conducted on an Empyrean instrument (PANalytical, Co., The Netherlands). Raman spectra were taken with aninVia confocal Raman Microscope (Renishaw Co., UK) with a 532 nm laser excitation. Nitrogen adsorption/desorption isotherms were obtained on a JW-BK200C (JWGB Sci. &Tech. Co., China), and before the measurement, the solid was completely dehydrated by heating at 200 °C for 6 h under vacuum. The samples used in SEM, XPS, XRD, Raman, and nitrogen adsorption/desorption isotherm analyses were freeze-dried.

Cs(I) adsorption tests

The adsorption experiment was conducted for the PB/rGOH by immersing it in Cs(I) solution with varied initial concentration of Cs(I). Except for specially stated, the dried weight of PB/rGOH was 9 mg, and the volume of Cs(I) solution was 15 mL. The solution pH was adjusted using HCl (5 M, 0.5 M, 0.05 M, and 0.005 M) or NaOH (5 M, 0.5 M, 0.05 M, and 0.005 M), and all the experiments were conducted at 25 °C with a shaking speed of 125 rpm. At the given time, the Cs(I) concentration in the supernatant was detected by inductively coupled plasma-atomic absorption spectrometry (ICP-AAS, ZEENT 700P, Analytikjena Co., Germany). The adsorption amounts of Cs(I) at equilibrium (q_e) and removal efficiency (RE) of Cs(I) were calculated according to eqn (1) and (2), respectively:

$$q_e = (C_0 - C_e)\frac{V}{m} \qquad (1)$$

$$RE\ (\%) = \frac{C_0 - C_e}{C_0} \times 100 \qquad (2)$$

where C_0 and C_e (mg L^{-1}) are the initial and residual concentration of Cs(I) in solution, respectively. V (L) is the volume of the aqueous solution, and m (g) is the adsorbent weight.

Results and discussion

Morphology

In the present study, we fabricated PB/rGOH by reducing GO using ascorbic acid in the presence of PB nanoparticles. Fig. 2a

shows the changes of the reaction system *versus* the reaction time. As the reduction time increased, the volume of mixed GO and PB nanoparticles shrunk greatly compared to its initial size and the blue-black suspension turned black, indicating that along with the reducing of GO, PB nanoparticles was embedded in the rGOH, and the self-assembled PB/rGOH formed. To examine the stability of the PB/rGOH, the hydrogel was shaken at 125 rpm for 72 h, and it still maintain an intact structure even after 72 h of shaking as shown in Fig. 2b. The SEM images of the freeze-dried rGO gel (Fig. 2c and d) and PB/rGO gel (Fig. 2e and f) show that rGO sheets display a smooth surface, while PB/rGO shows a rugged surface, confirming the adhering of PB nanoparticles on the surface of the rGO sheets. Both materials showed a well-defined and interconnected 3D porous network, and the pore sizes of the network were in micro scale. Taking advantage of their well-defined 3D porous structure, the rGOH and the PB/rGOH displayed a high water content of 99.67% and 98.54%, respectively. Such an interconnected 3D porous network could allow aqueous solution to flow through, ensuring effective mass transfer in the treatment of wastewater.

TEM images show that after reduction, rGO sheets stacked and formed the pore walls of the hydrogel (Fig. 3a, c and d). Meanwhile, different from the agglomerated state (Fig. 3b), PB nanoparticles were uniformly dispersed in the lamellar spacing of the rGO sheets (Fig. 3d). This could be possibly attributed to the improvement of the stability of PB nanoparticles due to the presence of rGO sheets in aqueous solution, and would be beneficial to the interaction between Cs(I) ions and PB nanoparticles, then facilitate the adsorption. As shown in Fig. 3e and f, the composite also exhibited strong mechanical strength, and the weight of the coin above the PB/rGOH were 1788 and 3577 times of the dry-weight of itself, respectively. The photographs of the PB/rGOH in Fig. 3g and h show that after drying the PB/rGOH shrunk to a stiff carbon bulk material, and the volume reduced to 1/125 of its initial volume.

Fig. 4 shows the N_2 adsorption/desorption isotherm and corresponding BJH pore-size distribution curve of the PB/rGOH. The isotherm revealed that the surface area of the composite was 98.21 $m^2 g^{-1}$, and the pore-sizes of the PB/rGOH was ranged from 2 to 10 nm (Fig. 4 inset). The composite exhibited a pattern closely related to the Type IV adsorption isotherm, according to
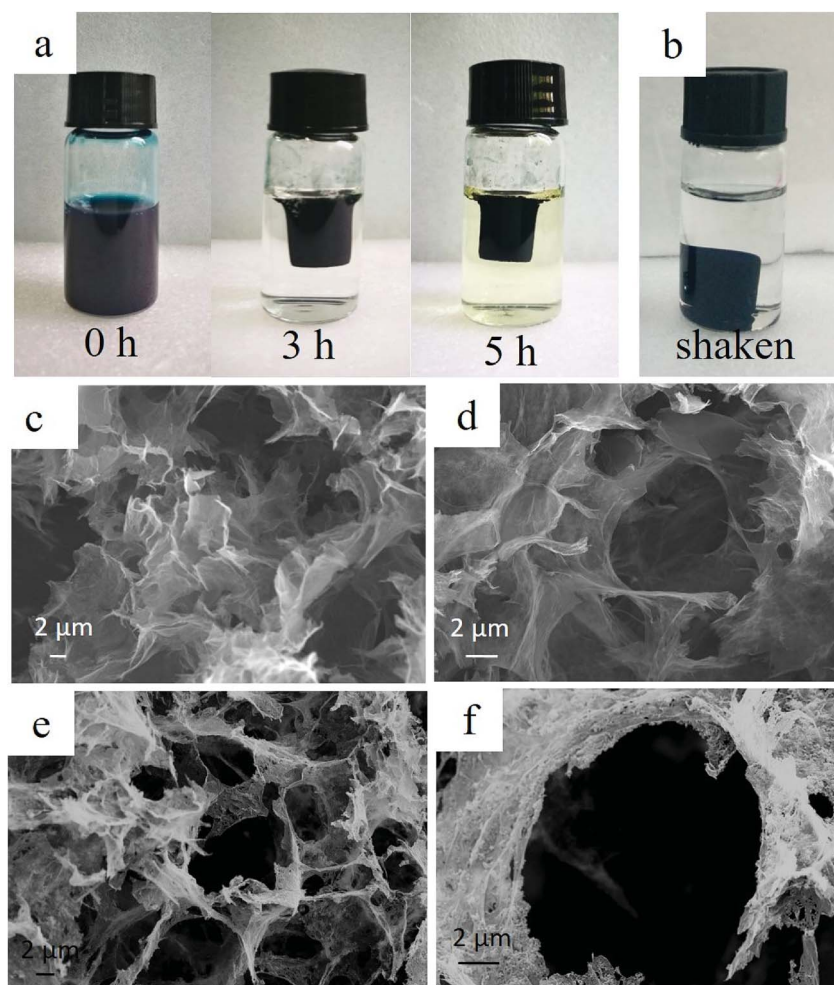

Fig. 2 (a) Images of the PB/rGOH at different reaction times; (b) image of the PB/rGOH after shaking for 72 h; (c, d) SEM images of the freeze-dried rGOH; and (e, f) SEM images of the freeze-dried PB/rGOH.
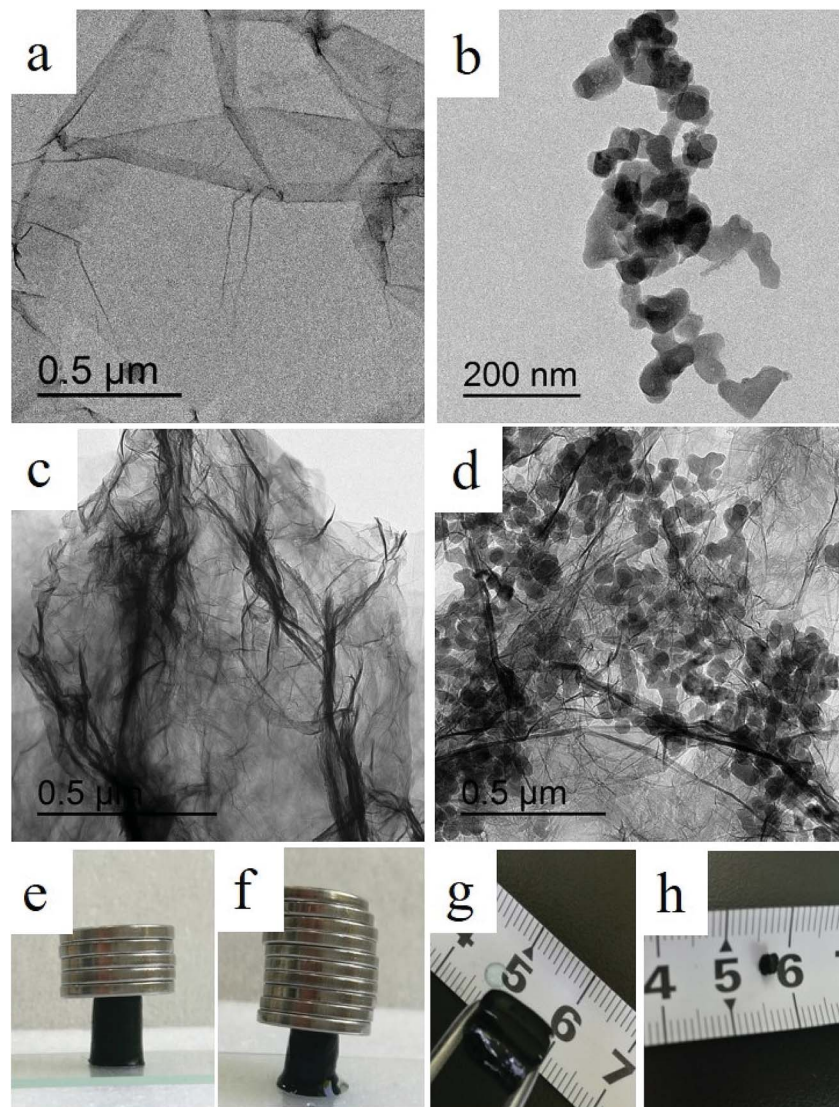
Fig. 3 TEM images of the GO (a), PB nanoparticles (b), rGO sheets (c), and PB/rGO sheets (d); (e and f) photographs of PB/rGOH allowing different supporting weight; (g and h) photographs of the PB/rGOH before and after natural air drying.

the IUPAC classification, and showed steep N_2 gas uptake at relatively low pressure region, indicating the mesoporous nature of the composite.[25]
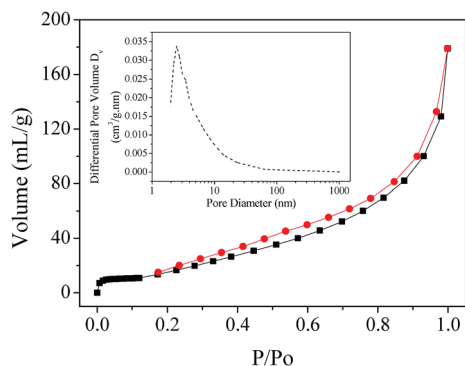

Fig. 4 Nitrogen adsorption/desorption isotherm of the PB/rGOH (inset: the pore-size distribution).

Chemical/physical properties

XPS analysis provided detailed information on the chemical composition of the as-prepared materials. The sharp peaks in the full scan spectrum of PB/rGOH revealed the presence of carbon, oxygen, nitrogen, and iron elements, and the relative oxygen content in rGO gel and PB/rGOH were significantly lower than that of GO (Fig. 5a). To further understand the electronic states of the elements, higher-resolution spectra of C 1s were also recorded (Fig. 5b–d). Four different peaks centered at 284.6, 285.5, 287.0, and 287.5 eV were observed in the C 1s deconvolution spectrum of GO, corresponding to C=C sp^2, C–C sp^3, C–O, and C=O, respectively (Fig. 5b). The spectrum of the rGOH (Fig. 5c) shows three peaks located at 284.4, 285.8, and 288.4 eV, respectively. The ratio of the oxygen containing groups decreased significantly, confirming the reduction of the GO. For the PB/rGO, Fig. 5d only shows C≡N and matrix C–C peaks at 285.5 and 284.5 eV, respectively.[26] These results indicate that
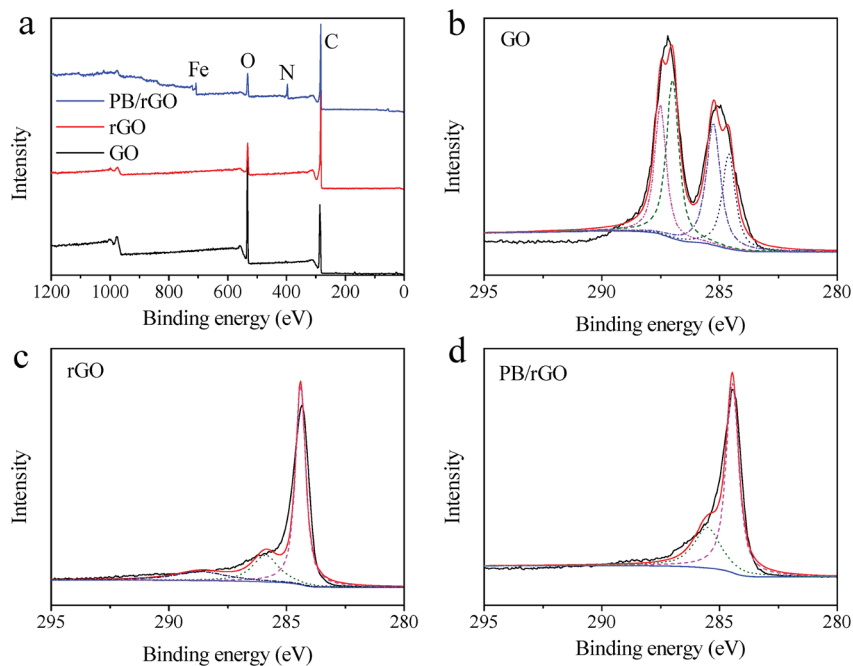
Fig. 5 Full scan XPS spectra of (a) GO, rGO, and PB/rGOH; (b) C 1s spectra of GO; (c) C 1s spectra of rGOH; and (d) C 1s spectra of PB/rGOH.

GO was effectively reduced to rGO, and PB nanoparticles were assembled in rGOH during the reduction process.

Fig. 6a shows the XRD patterns of GO, rGOH, PB, and PB/rGOH. The characteristic 2θ peak for the rGOH appeared at 23.11°, corresponding to an interlayer spacing of 0.384 nm. This value was much lower than that of GO (0.881 nm), suggesting the existence of π–π stacking interaction between rGO sheets in the network, and further demonstrated the effective reduction of GO. The pattern of the PB/rGOH shows almost the same characteristic peaks with PB, which might be attributed to the low content of rGO in the material.

Raman spectra show the existence of D-band and G-band in GO, rGOH, and PB/rGOH (Fig. 6b). The D-band is attributed to A_{1g} photon of sp^3 carbon atoms of disordered graphite, and the G-band is related to the in-plane vibration of sp^2 carbon atoms. The G-band of GO was located at 1593 cm^{-1}, while that of rGOH was red shifted to 1588 cm^{-1}, closing to the value of the pristine graphite,[27] suggesting the elimination of oxygen containing groups and the enhancement of the gelation. However, the G-band of PB/rGOH was blue shifted to 1592 cm^{-1}, because the assembling of PB into the rGOH hindered the π–π stacking interaction and inhibited the gelation of rGOH.

GO contains many oxygen-containing functional groups on its surface, making it well dispersed in water. However, the reduction of GO could diminish the oxygenated groups on its surface and restore its conjugated domains, as evidenced by the XPS, XRD, and Raman spectra. Driven by the hydrophobic and π–π stacking interaction of the conjugated structure, the cross-linking through partial overlapping of the rGO sheets occurs, and the volume gradually shrinks, accompanying with the embedding of PB nanoparticles inside. Finally, the sufficient cross-linking sites are generated for forming a 3D network. The
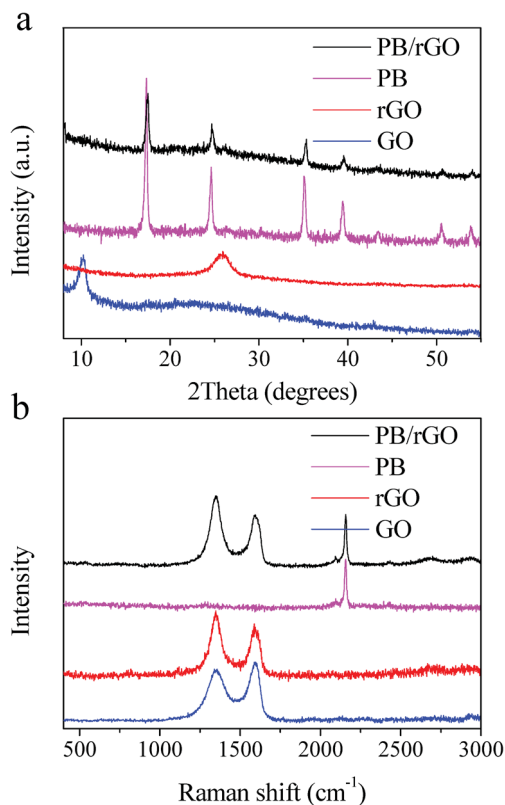

Fig. 6 XRD (a) and Raman spectra (b) of the GO, PB nanoparticles, rGOH, and PB/rGOH.

PB nanoparticles can be captured by the rGOH in two approaches: firstly, when PB nanoparticles were mixed with GO suspension, some nanoparticles could be fixed on the surface of
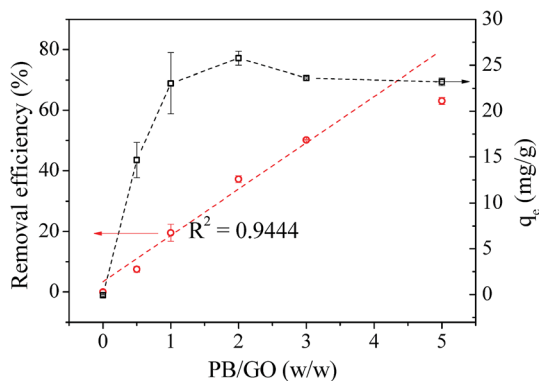
Fig. 7 The influence of the ratio of PB/GO (w/w) on the adsorption performance of the composites. 15 mL of 100 mg L^{-1} Cs(I) was added into 20 mL glass bottle containing PB/rGOH, pH = 5, T = 25 °C, and the Cs(I) concentration of the supernatant was detected after 72 h.

GO by forming new bonds between PB and GO due to the abundant oxygenated groups of GO, and these nanoparticles were retained onto the surface of the rGO sheets by chemical attachment after GO was reduced. This process is similar to the reported method for preparing PB/RGO hybrids.[28] Secondly, there are still more PB nanoparticles dispersed in the mixed suspension, which can be captured by the physical entrapment (between rGO sheets) during the formation of the 3D architecture.[29]

The development of nuclear industry inevitably results in more and more production of radioactive wastewater. Radionuclide is a kind of specific pollutant, because its hazardness and toxicity cannot be changed by chemical and physical approaches. Isolation and its spontaneous decaying to stable nuclide is the only way to avoid irradiation hazard. Therefore, it is quite necessary to reduce the volume of the radioactive waste. After totally desiccated, the strong π–π stacking interaction between the rGO sheets makes the PB/rGOH further shrink to form graphite-like bulk materials,[30] which is conducive for further reducing the volume of wastewater and will be beneficial to the waste minimization.

Adsorption experiments

The influence of PB/GO (w/w) ratio on the Cs(I) adsorption performance of PB/rGOH was validated (Fig. 7). When the PB/GO ratios were set 0, 0.5, 1, 2, 3, 5 in the preparation, the dried weights of the composites were 3 mg, 6 mg, 9 mg, 16 mg, 22 mg, and 30 mg, respectively. To conduct the Cs(I) adsorption experiments, the whole piece of hydrogel were put into the Cs(I) aqueous solution. As shown in Fig. 7, the RE continuous increased with the increase of the PB/GO ratio. Meanwhile, in the absence of PB, rGOH shows no adsorption of Cs(I), and the Cs(I) removal efficiency of the PB/rGOH approximately follows a linear relationship with the ratio of PB/GO. This result indicates PB played the role of adsorbing Cs(I), while rGOH only acted as a support assembling for PB nanoparticles. The adsorption capacities of the composite increased along with the increase of PB/GO ratio when it was lower than 2 and decreased slightly when the PB/GO ratio was further increased. It is possible that when the ratio of PB/GO is
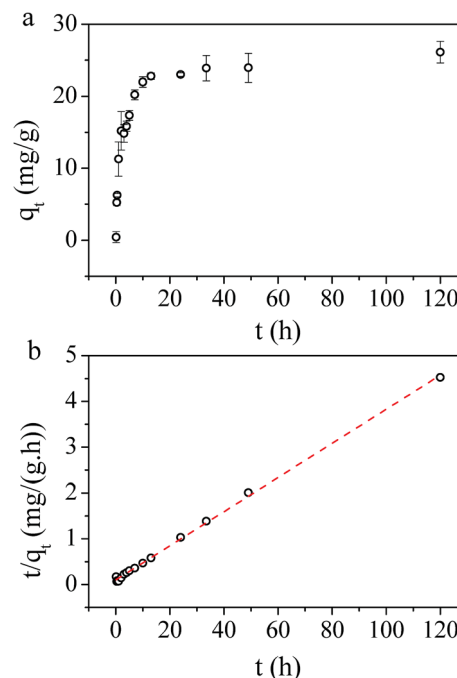

Fig. 8 (a) Influence of time on adsorption performance, and (b) adsorption kinetic plots of t/q_t vs. t. The dried weight of the PB/rGOH was 9 mg, Cs(I) concentration was 40 mg L^{-1} (15 mL), pH = 4, T = 25 °C.

low, the weight of the rGO accounts a large share of the composite, which decreases the adsorption capacity of PB nanoparticles itself. However, as the PB/GO ratio further increased, the weight proportion of the rGO become smaller, so the adsorption capacity of the composite got closer to that of the PB nanoparticles. Meanwhile, it was found that PB/rGOH were stable after 72 h of shaking when the ratio of PB/GO was lower than 2, while the ratio of PB/GO is higher than 2, there would be some PB nanoparticles released by the rGOH. So, from a stability point of view, the PB/GO ratio of 1 was used in the followed experiments.

The effect of contact time on the Cs(I) adsorption of PB/rGOH is presented in Fig. 8a. A rapid uptake of Cs(I) ions was observed after addition of PB/rGOH, and about 50% of the equilibrium adsorption capacity was reached within the first 2 hours, while 10 hours were sufficient to achieve 85% of the equilibrium adsorption capacity. The equilibrium time for Cs(I) adsorption needed by PB/rGOH was longer than that by PB nanoparticles, which was due to the limited mass transfer rate in the hydrogel.[31] However, this value was comparable with those studies in which PB nanoparticles were embedded into chitin beads, alginate/calcium beads, etc.[32,33]

In order to understand the dynamics of the adsorption process, kinetic data were analyzed using pseudo-first-order and

Table 1 Rate constants and correlation coefficients of the pseudo-second-order kinetic model

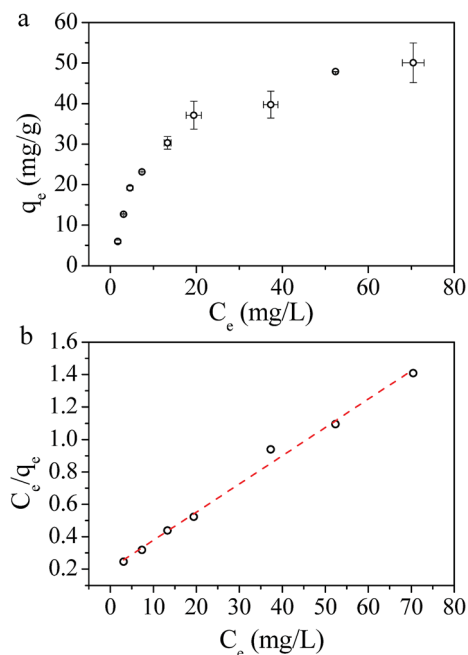|	q_e (mg g^{-1})	k_2 (g (mg h)$^{-1}$)	V_0 (mg (g h)$^{-1}$)	R^2
PB/rGOH	26.83	0.0135	9.74	0.99

Fig. 9 (a) Influence of concentration on adsorption performance, and (b) Langmuir isotherms. The dried weight of the PB/rGOH was 9 mg, the volume of Cs(I) were 15 mL, and pH = 5, $T = 25\ °C$, $t = 72$ h.

pseudo-second-order kinetics. The results in our work perfectly follows pseudo-second-order kinetic model, which is expressed as:

$$\frac{t}{q_t} = \frac{1}{k_2 q_e^2} + \frac{t}{q_e} \tag{3}$$

where q_t is the amount of adsorbed pollutant on per unit weight of adsorbent (mg g^{-1}) at time t (h), q_e is the sorption capacity at equilibrium (mg g^{-1}), and the parameter k_2 (g (mg h)$^{-1}$) represents the pseudo-second-order rate constant for the kinetic model. The fitting of the experimental data to the pseudo-second-order model ($R^2 = 0.995$) suggested that Cs(I) adsorption on PB/rGOH is a chemisorption rather than a physisorption (Table 1 and Fig. 8b).[34] Calculated from the fitting results, the values of q_e and k_2 were obtained as 26.83 mg g^{-1} and 0.0135 g (mg h)$^{-1}$, respectively. From these values, the initial adsorption rate of 9.74 g (mg h)$^{-1}$ was calculated using the equation $V_0 = k_2 q_e^2$.[35]

Adsorption isotherm can provide information about adsorption mechanisms, surface properties, and the affinity of the adsorbent towards the adsorbate. In this study, the adsorption of Cs(I) ions with different initial concentrations were studied at 298 K and pH = 5, with an adsorption time $t = 72$ h (Fig. 9a). To explore the adsorption mechanism, we validated the relationship between adsorbed cesium and its residual in aqueous solution at adsorption equilibrium

Table 2 Langmuir isotherm constants and their correlation coefficients

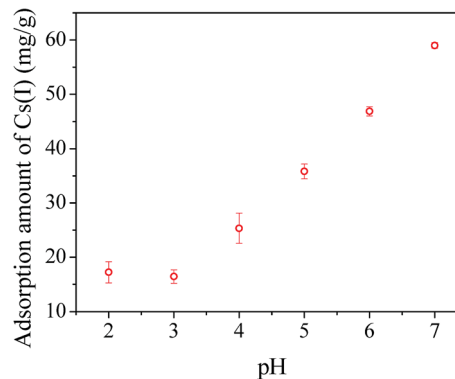|	Q_{max} (mg g^{-1})	b (L mg^{-1})	R^2
PB/rGOH	58.82	0.0837	0.99

Fig. 10 Influence of pH on adsorption capacity. The dried weight of PB/rGOH was 9 mg, Cs(I) concentration was 40 mg L^{-1} (15 mL), $T = 25\ °C$, $t = 72$ h.

according to the Langmuir model and Freundlich model. The experimental adsorption data fitted well with Langmuir isotherms (Fig. 9b), suggesting that the adsorbent surface was heterogeneous in nature. The linear form of the Langmuir isotherm is represented by:

$$\frac{C_e}{q_e} = \frac{1}{Q_{max}b} + \frac{C_e}{Q_{max}} \tag{4}$$

where C_e (mg L^{-1}) is the equilibrium concentration of Cs(I), q_e (mg g^{-1}) is the equilibrium sorption capacity of the adsorbent, b is the Langmuir constants relating to the energy of adsorption (L mg^{-1}), and Q_{max} is the maximum adsorption capacity (mg g^{-1}). The Langmuir isotherm constants and their correlation coefficients for PB/rGOH are listed in Table 2. The Q_{max} value for PB/rGOH is 58.82 mg g^{-1}, which is comparable with many PB-based adsorbents reported previously.[26,36] However, this value is lower than the value of PB functionalized Fe$_3$O$_4$ (280.82 mg g^{-1}),[13] but higher than that of PB/RGOF reported by Jang et al. (18.67 mg g^{-1}).[25] This could be mainly attributed to the difference of the size of the nanoparticles and the surface area of the composites.[13,37] The surface area of PB/rGOH in our work was 98.21 m^2 g^{-1}, and the size of the PB was 50–100 nm; while the PB/Fe$_3$O$_4$ mentioned above had surface area of 332.19 m^2 g^{-1} and size of 13.9 nm, and the PB/RGOF in ref. 25 showed a surface area of 43.07 m^2 g^{-1}.

pH value is one of the most important parameters affecting the adsorption capacity. In this study, experiments were conducted at different pH values from 2 to 7. As shown in Fig. 10, the Cs(I) adsorption capacity of PB/rGOH gradually increased with elevated pH values from 3.0 to 7.0, which could be attributed to that the adsorption of Cs(I) was suppressed due to the competition of H$_3$O$^+$.[26,38] Further increasing the pH value resulted in serious decomposition of PB nanoparticles in our study, which interfere the measurement. The low stability of the PB was due to the strong interaction between ferric ions and hydroxyl ions at alkaline condition, which resulted in Fe–CN–Fe bond cleavage in PB.[39,40]

Conclusions

In the present work, we have successfully developed PB/rGOH for Cs(I) removal. The as-prepared materials displayed a 3D

porous network, and the PB nanoparticles distributed uniformly on the rGO sheets. The materials could be separated easily from aqueous solution. Moreover, the volume of the hydrogel could shrink to one in 125 of its initial volume after natural air dry, which will be beneficial for the waste minimization. It was demonstrated that in the PB/rGOH, the Cs(I) adsorption was dominated by PB nanoparticles, and the rGOH played the role of supporting substrate and making it easy to separate from water. The Cs(I) adsorption performance of the PB/rGOH fitted well with the pseudo-second-order kinetic and the Langmuir isotherm model, and an maximum adsorption capacity of 58.82 mg g^{-1} was obtained. In addition, we also found that Cs(I) adsorption significantly depends on the pH of solution. These results demonstrated that the PB/rGOH have a good application prospect in radioactive waste water treatment.

Conflicts of interest

There are no conflicts to declare.

Acknowledgements

References

1 http://www.iea.org/publication/freepublications/publication/keyworld2016.pdf.

2 M. J. Manos and M. G. Kanatzidis, *J. Am. Chem. Soc.*, 2012, **134**, 16441–16446.

3 J. Johnson, *Chem. Eng. News*, 1998, **76**, 25–27.

4 S. Merz, K. Shozugawa and G. Steinhauser, *Environ. Sci. Technol.*, 2015, **49**, 2875–2885.

5 M. R. Awual, S. Suzuki, T. Taguchi, H. Shiwaku, H. Okamoto and T. Yaita, *Chem. Eng. J.*, 2014, **242**, 127–135.

6 S. Y. Ding, Y. Yang, H. O. Huang, H. C. Liu and L. A. Hou, *J. Hazard. Mater.*, 2015, **294**, 27–34.

7 C. Vincent, Y. Barre, T. Vincent, J. M. Taulemesse, M. Robitzer and E. Guibal, *J. Hazard. Mater.*, 2015, **287**, 171–179.

8 L. Chang, S. Chang, W. Chen, W. Han, Z. Li, Z. Zhang, Y. Dai and D. Chen, *RSC Adv.*, 2016, **6**, 96223–96228.

9 D. R. Melo, J. L. Lipsztein, C. A. N. Oliveira and L. Bertelli, Radiation Protection/Medical Aspects of the Goiania Accident, Individual Monitoring, *REMPAN 97*, 1997, pp. 185–188.

10 S. Feng, X. Li, F. Ma, R. Liu, G. Fu, S. Xing and X. Yue, *RSC Adv.*, 2016, **6**, 34399–34410.

11 M. Darder, *RSC Adv.*, 2014, **4**, 35415–35421.

12 J. Qian, J. Ma, W. He and D. D. Hua, *Chem.–Asian J.*, 2015, **10**, 1738–1744.

13 J. Jang and D. S. Lee, *Ind. Eng. Chem. Res.*, 2016, **55**, 3852–3860.

14 A. K. Vipin, B. Fugetsu, I. Sakata, A. Isogai, M. Endo, M. Li and M. S. Dresselhaus, *Sci. Rep.*, 2016, **6**, 37009–37022.

15 H. Yang, L. Sun, J. Zhai, H. Li, Y. Zhao and H. Yu, *J. Mater. Chem. A*, 2013, **2**, 326–332.

16 Y. Huang, M. Zeng, Z. Feng, D. Yin, Q. Xu and L. Fan, *RSC Adv.*, 2016, **6**, 3561–3570.

17 A. Pourjavadi, M. Nazari, B. Kabiri, S. H. Hosseini and C. Bennett, *RSC Adv.*, 2016, **6**, 10430–10437.

18 C. Du, Z. Yao, Y. Chen, H. Bai and L. Li, *RSC Adv.*, 2014, **4**, 9133–9138.

19 M. Gao, C. K. N. Peh, L. O. Wei and G. W. Ho, *RSC Adv.*, 2013, **3**, 13169–13177.

20 W. Li, Y. Ye, X. Lu, W. Yi, L. Sun, H. Tan, F. Xu and Y. Song, *Electrochim. Acta*, 2013, **114**, 223–232.

21 H. Q. Gong, M. H. Sun, R. H. Fan and L. Qian, *Microchim. Acta*, 2013, **180**, 295–301.

22 B. Adhikari, A. Biswas and A. Banerjee, *ACS Appl. Mater. Interfaces*, 2012, **4**, 5472–5482.

23 Z. Zhang, T. Sun, C. Chen, F. Xiao, Z. Gong and S. Wang, *ACS Appl. Mater. Interfaces*, 2014, **6**, 21035–21040.

24 Y. Xu, H. Bai, G. Lu, C. Li and G. Shi, *J. Am. Chem. Soc.*, 2008, **130**, 5856–5857.

25 S. C. Jang, Y. Haldorai, G. W. Lee, S. K. Hwang, Y. K. Han, C. Roh and Y. S. Huh, *Sci. Rep.*, 2015, **5**, 17510–17519.

26 H. J. Yang, L. Sun, J. L. Zhai, H. Y. Li, Y. Zhao and H. W. Yu, *J. Mater. Chem. A*, 2014, **2**, 326–332.

27 W. Chen and L. Yan, *Nanoscale*, 2011, **3**, 3132–3137.

28 N. Zhu, S. Han, S. Gan, J. Ulstrup and Q. Chi, *Adv. Funct. Mater.*, 2013, **23**, 5297–5306.

29 W. F. Chen, S. R. Li, C. H. Chen and L. F. Yan, *Adv. Mater.*, 2011, **23**, 5679–5683.

30 Y. Xu, Z. Lin, X. Huang, Y. Wang, Y. Huang and X. Duan, *Adv. Mater.*, 2013, **25**, 5779–5784.

31 M. Ishizaki, S. Akiba, A. Ohtani, Y. Hoshi, K. Ono, M. Matsuba, T. Togashi, K. Kananizuka, M. Sakamoto and A. Takahashi, *Dalton Trans.*, 2013, **42**, 16049–16055.

32 A. K. Vipin, B. Hu and B. Fugetsu, *J. Hazard. Mater.*, 2013, **258–259**, 93–101.

33 T. Vincent, C. Vincent, Y. Barré, Y. Guari, G. L. Saout and E. Guibal, *J. Mater. Chem. A*, 2014, **2**, 10007–10021.

34 A. A. Kadam, J. Jang and D. S. Lee, *Bioresour. Technol.*, 2016, **216**, 391–398.

35 H. Faghihian, M. Moayed, A. Firooz and M. Iravani, *J. Colloid Interface Sci.*, 2013, **393**, 445–451.

36 H. Yang, H. Li, J. Zhai, L. Sun, Y. Zhao and H. Yu, *Chem. Eng. J.*, 2014, **246**, 10–19.

37 D. Parajuli, A. Kitajima, A. Takahashi, H. Tanaka, H. Ogawa, Y. Hakuta, K. Yoshino, T. Funahashi, M. Yamaguchi and M. Osada, *J. Environ. Radioact.*, 2016, **151**, 233–237.

38 T. Sangvanich, V. Sukwarotwat, R. J. Wiacek, R. M. Grudzien, G. E. Fryxell, R. S. Addleman, C. Timchalk and W. Yantasee, *J. Hazard. Mater.*, 2010, **182**, 225–231.

39 F. Ricci, A. Amine, G. Palleschi and D. Moscone, *Biosens. Bioelectron.*, 2003, **18**, 165–174.

40 J. Jang and D. S. Lee, *Bioresour. Technol.*, 2016, **218**, 294–300.